The Search for Efficient and Stable Metal-Organic Frameworks for Photocatalysis: Atmospheric Fixation of Nitrogen

Amro M.O. Mohamed, Yusuf Bicer

Applied Surface Science 583 (2022) 152376

Contents lists available at ScienceDirect

Applied Surface Science

journal homepage: www.elsevier.com/locate/apsusc

Full Length Article

The Search for Efficient and Stable Metal-Organic Frameworks for Photocatalysis: Atmospheric Fixation of Nitrogen

Amro M.O. Mohamed *, Yusuf Bicer

Division of Sustainable Development, College of Science and Engineering, Hamad Bin Khalifa University, Qatar Foundation, Doha, Qatar

ARTICLE INFO

Keywords:
Computational screening
Electronic properties
Green ammonia
Life cycle assessment
Molecular simulation
Photoactivity
Solar energy

ABSTRACT

Recent research targets the low-pressure synthesis of ammonia via a light-initiated catalytic process. Despite the importance of materials selection for photocatalysis, computational efforts to guide candidate materials' nomination ahead of experiments are lacking. The purpose of this study is to employ computational screening, using density functional theory and molecular simulations, to select and evaluate metal–organic frameworks (MOFs) as nitrogen fixation photocatalysts and further deduce correlations for the prediction of MOFs' electronic properties. First, MOFs with appropriate electronic and structural properties are identified. The top candidates have been examined from the perspective of adsorption, diffusion, and mechanical and chemical stability properties. Four MOFs, Fe_2Cl_2(BBTA), Fe_2(mDOBDC), Zn_2(mDOBDC), and Ni-BTP, have been selected based on their band edges, while only Fe_2Cl_2(BBTA) MOF exhibited a bandgap less than 3 eV. Fe_2(mDOBDC) exhibited the highest shear modulus of approximately 31 GPa. In addition, a life cycle assessment of the four MOFs showed that Ni-BTP has the lowest environmental impact. A set of 48 MOFs' combinations are proposed for heterojunction application to enhance charge carriers' separation. Intriguingly, we demonstrated the predictability of MOF's bandgap and edges from MOF's organic linker bandgap and metal node type (oxidation state and corresponding electronic configuration) for MOF families.

1. Introduction

Carbon-free systems are sought-after by the transition into a hydrogen-oriented and more sustainable economy. Total elimination of carbon from the chemical industry may be impracticable since carbon is the core of petrochemical compounds and products. One of the primary challenges hindering the worldwide hydrogen economy's employment is the supply chain's storage and transportation challenges. Ammonia has been presented as a hydrogen vector as it addresses the problems associated with hydrogen storage, safety, and integration in the transportation industry. The carbon-free chemical, ammonia, is one of the most produced chemicals worldwide, reflecting the handling experience while maintaining high energy and hydrogen content.

The ammonia produced in the world relies primarily on implementing the methane steam reforming followed by the Haber-Bosch process, which is broadly known to be highly pollutant and consumes high energy [1]. Several strategies have been proposed to reduce the carbon emissions and energy consumption of ammonia production [1]. These include thermochemical, electrochemical, and enhanced Haber-Bosch processes [1,2]. A process that is envisioned to be more sustainable and environmentally benign is the photocatalysis route. The photocatalysis process combines catalysis and photoactivity aspects of materials to utilize solar energy efficiently. Photocatalysis has been introduced to various applications, one of which is the water-splitting process to produce hydrogen. Developing efficient photocatalysts increases processes' sustainability inherently from an energy intensity perspective and uses renewable energy sources.

Due to the enormous number of Metal-Organic Frameworks (MOFs) provide a range of electronic properties, making them candidates materials for various photosensitive-based applications. These applications include; sensing [3], water splitting [4,5], nitrogen reduction, fuel cells [6], and degradation of organic materials pollutants [7], in addition to other various applications, including supercapacitors [8]. Besides the applications mentioned above, MOFs are introduced in various applications, including gas separation, catalysis, and selective adsorption [9]. MOFs screening practice focused on gas separation applications, especially CO_2 capture-related applications [10]. The studies, in general, targeted the generation of structural/property relationships. Several

* Corresponding author.
E-mail address: ammohamed@hbku.edu.qa (A.M.O. Mohamed).

https://doi.org/10.1016/j.apsusc.2021.152376
Received 18 June 2021; Received in revised form 25 December 2021; Accepted 27 December 2021
Available online 7 January 2022

correlations and trends have been established. Among these are working capacity versus surface area, uptake versus heat of adsorption, and selectivity performance versus most structural properties. On the other hand, a handful of limitations are known with such methodologies, including representation of host-adsorbate interactions, assumption of an ideal-defect-free structure, and stability of structures are not necessarily guaranteed.

Several research teams have studied the implementation of photoactive materials towards ammonia production using several material classes [11]. Recently, MOFs have been proposed as candidates for the nitrogen fixation process [12]. MOFs can be ideal catalysts due to the material's crystalline nature and can create a platform for custom-made artificial enzymes. There are several reasons why MOFs are considered a potential candidate for the applications. A reason is that MOFs are rich in terms of properties' alteration; via metal replacement, the substitution of organic ligands, and functionalization [13].

There is a rapidly growing research interest in examining the effectiveness of MOFs in the photofixation of nitrogen. The work produced by Huang et al. constitutes an experimental work that investigated MIL-125 (Ti) based MOFs for applying nitrogen fixation [14]. Among the type of functionalization examined, the amino group functionalized showed the highest activity. The observed rate of ammonia produced is 12.25 μmol $g^{-1}h^{-1}$. A different set of MOFs was scrutinized using a similar experimental setup for the same application. Li et al. studied nitrogen's photofixation using Fe-based MOFs in MIL-101(Fe), MIL-100(Fe), and MIL-88(Fe), in addition to MIL-101(Cr) [15]. It was reported that higher ammonia production using MIL-101(Fe) reached 1007.1 μmol $g^{-1}h^{-1}$. The research work was accompanied by a computational effort to explain some questions related to materials' effectiveness. Photoelectric current and electrochemical impedance spectroscopy were carried out and showed that higher current density is achievable with Fe atom.

Furthermore, a nitrogenase-inspired MOF in MIL-53(Fe^{II}/Fe^{III}) was first synthesized and evaluated for nitrogen fixation under visible light [16]. The stable MOF with an optimal Fe^{II}/Fe^{III} ratio of 1.06:1 yielded 306 μmol $g^{-1}h^{-1}$. The enzyme exhibits superior nitrogen fixation efficiency due to the presence of the multi-iron metallocluster. The study indicated the importance of charge mobility in the system and incorporating biological understanding in synthesizing new materials. In addition to the experimental work, the authors proposed a mechanism under which the process occurs. Moreover, Ding et al. combined the excellent non-metallic catalyst graphite C_3N_4 with MOF-74 (Zn-BDC-based MOF) throughout a sol–gel method [17]. Incorporating these materials introduces the effective Z-scheme mechanism to facilitate nitrogen photo-based fixation. The bandgap of bulk C_3N_4 is 2.62 eV. It is expected that such systems would effectively separate charge carriers and avoid undesired charge carriers recombination.

Our previous paper has introduced a methodology that combines several descriptors to select MOFs from primary databases [18]. The criteria include photosensitivity, structural, geometrical, diffusion, and adsorption properties of MOFs. It is important to note that we integrated other sustainability matrices such as life cycle assessment to quantify and compare materials from an environmental perspective. A case study was conducted on the Hypothetical MOFs (HMOFs) database [18]. The study highlighted the importance of understanding the database and the role of three significant effects in MOFs, linker, metal, and functionality. The functionality effect was represented mainly by the functional group list used to construct the database. The selected structure, based on a functionlized BTC linker, was compared to MIL-125(Ti) from adsorption, diffusion, and electronic properties (bandgap), besides estimating these materials' environmental burdens.

The previous work showed the capability of functionalization to effectively alter light absorption activity for the particular photoreaction [18]. However, we noted that the database was limited and more diverse, and experimental-based databases had to be screened for analysis and to provide a reasonable understanding of the significant trends to reach predictive modeling. Also, it is important to include parameters on charge separation and mobility to enhance the selection process. In this work, a dataset - based on open metals MOFs - is screened for the application alongside a preliminary screening of computation-ready experimental (CoRe) MOFs (Chung et al., 2014) and combined results HMOFs for further comparisons and analyzes. Simulations are incorporated to nominate appropriate materials from various aspects, including electronic, chemical, energetic, and mechanical stabilities. Understanding both the metal and linker's role in overall photosensitivity is highlighted in this work, where correlations are built to predict MOFs' bandgap and band edges.

1.1. Significance of the present study

The work aims to select appropriate MOFs for the photofixation of nitrogen to produce ammonia using computational tools. The selection of MOFs towards photocatalysis applications is desired due to low product yields. We incorporate electronic properties and include molecular transport phenomena coefficients and stability. This paper incorporates life cycle thinking of the material synthesis and compares the environmental impact of MOF production. MOF-MOF heterojunction is also proposed to identify opportunities to extend the lifetime of photogenerated charges. The study also includes establishing correlations that predict MOFs bandgap and band edges. Our findings reveal a strong correlation between organic linker bandgap and metal type in determining structure bandgap. One of the main targets of this work is to translate predictive computational chemistry tools to select efficient photocatalysts for various applications. Outcomes from this research paper can be used as a cornerstone to prepare specific MOF databases for photoactivity and guide and complement experimental work in the field.

Fig. 1 depicts the main building blocks in this piece of work; (1) screening of MOFs for desired properties for photocatalysis of nitrogen reduction, (2) proposing direct heterojunction MOFs, and (3) construct models to correlate MOFs' electronic properties from its constitutes. This work's scope should direct future databases specific towards photoactive applications and experiments for efficient nitrogen reduction with MOFs.

2. Methodology

2.1. Databases and overall screening methodology

The dataset used in this work was built by Rosen et al. [19] for methane activation application. It contains various structures and linkers. A total of 60 structures are presented in this dataset which was chosen because at least one family member has been shown to support open metal sites that are redox-active [19]. In addition, a partial computational ready database was used to screen for more potential MOFs. The structures are collected from CSD, assuming they were correct. Solvents and coordinated solvents were removed from the structure, and charge-balancing ions were added from neutrality [20]. CoRE MOFs were screened for necessary structural properties, and then only Fe-based MOFs were studied for electronic properties [21].

2.2. Desired electronic properties

The primary electronic properties in question are the bandgap and position of band edges. For the desired electron transfer reaction to occur, the electron acceptor species' potential should be located below (more positive than) the semiconductor's conduction band. In contrast, the electron donor species' potential should be located above (more negative than) the semiconductor's valence band. Thus, the amount of captured solar light (bandgap function) and band positions are considered the most important. The captured light corresponds to the solar spectrum's integration to the bandgap corresponding wavelength.

CP2K/QUICKSTEP package was utilized to perform electronic Density Functional Theory (DFT) computations on the MOFs in this study

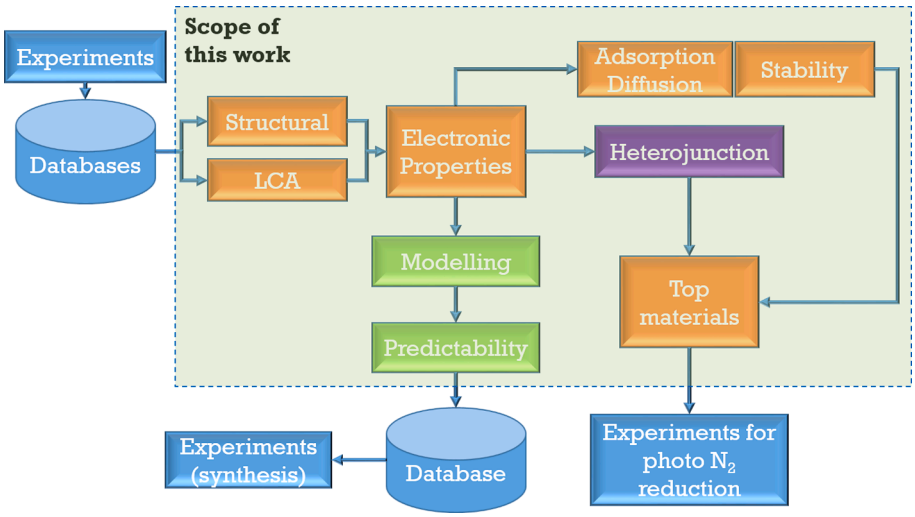

Fig. 1. Scope of this research work on the screening of MOFs for photocatalytic nitrogen reduction to produce ammonia.

[22,23]. DFT computations have been carried out at Perdew Burke Ernzerhof (PBE) [24] and HSE06 level of theory for comparison purposes. The hybrid functional HSE06, at a screening parameter of 0.11 [25], was used primarily in this work for better determination of bandgap. Hybrid functionals are known to solve underestimation typically presented with generalized gradient approximation (GGA) functionals and thus provide improved results regarding bandgaps of semiconductors. The mixing parameter of Hartree-Fock was set to 0.25, and the method of auxiliary density matrix methods (ADMM) was implemented in the HF exchange [26]. Core electrons were represented by Goedecker Teter Hutter (GTH) PBE pseudopotentials [27,28]. The optimized Gaussian basis sets (MOLOPT) are used [29] DZVP-MOLOPT-SR contracted Gaussian basis sets for solids and an auxiliary plane-wave basis set. Band edges were aligned to the standard hydrogen electrode, as demonstrated by Liu et al. [30]. Band edges were adjusted to SHE using $U^{\circ}_{(H^+/H_2)}$ (periodic boundary conditions) = 0.81 V following discussion in the cited publication. The target accuracy for all SCF convergences is 1.0E-6.

This work uses a solid-state perspective where periodic boundary conditions were used in determining MOF's electronic properties. The design criteria of the bandgap should be between 2.75 and 3.00 eV. The lower limit is estimated as the gap required for nitrogen fixation from water as the proton source of 2.49 eV plus 0.25 eV. The lower limit realistically may have to be even higher. The higher limit is fixed at 3.00 eV to ensure better light absorption properties. This work relates the amount of light captured by the MOF from the fundamental band gap obtained from DFT computations (integration of solar spectrum, see Figure S1). It is essential to highlight that the difference between fundamental and optical gaps was significant in some MOFs because of non-negligible exciton binding energies [31]. The electron transfer reaction's efficiency is a function of the semiconductor's conduction and valence band edges relative to the adsorbed substrate's redox potential [32]. Concerning the band position, the following pair of inequalities must be satisfied for a material to be considered.

$$VB_{edge} > 1.23V \text{ vs SHE and } CB_{edge} < -1.26V \text{ vs SHE}$$

The rationale of the band edges selected evaluated from oxygen evolution reaction at the highest occupied molecular orbital (HOMO) level, and conduction band is associated with non-dissociative nitrogen fixation as previously studied two electrons reduction associative pathway mechanism [18]. Table S1 lists the reduction process steps of nitrogen to ammonia with the potential of reactions at 298 K versus the standard hydrogen electrode (SHE). Several challenges are considered when designing semiconductors for photocatalysis application, including the low kinetic barrier for the electron-hole recombination process and finding the right band edges to facilitate the redox reaction. Therefore, a study is implemented where the density of state (DOS) computations are carried out. Obtaining DOS is relevant to observe electronic states' availability in the middle between the determined conduction band and the Fermi level using Fermi-Dirac distribution at an electronic temperature of 300 K.

Another critical parameter to determine the efficiency of photocatalytic materials is charge carrier effective mass (m^*) which is used to reflect on the photoconductive properties and the mobility of the charge carriers [33]. The effective masses of charge carriers are estimated by fitting a parabola of the obtained band structure using PBE functional. The reciprocal space path, compatible with space group symmetry within the Brillouin zone, was computed using the Seek-path package [34]. In this work, we used the relative effective mass of the hole to the electron (D) to characterize charge separation as adopted in other works [35].

$$D = \frac{m^*_h}{m^*_e} \tag{1}$$

$$m^* = \hbar^2 \times \left(\frac{\partial^2 E}{\partial k^2}\right)^{-1} \tag{2}$$

Where k is the wavevector and $\hbar$ is the reduced plank constant, and E is the energy of an electron at wavevector k in the band. The relative effect mass ratio compares a potential candidate for the photocatalytic process.

A typical discussion is raised on predicting the desired property from structural or geometrical properties from a MOFs' screening procedure. Here, we attempted to estimate the electronic properties of a MOF from its constitutes, namely the organic linker and metal node. Predicting bandgap and band edges are accomplished for a selected number of MOFs' families. They should provide a property-property and a structure–property relationship of electronic bandgap and band edges of MOFs. The organic linkers were extracted from the structure file of corresponding MOFs containing the linker for the DFT computations. Hydrogen atoms were added to the organic compound manually with no additional equilibration as the structures were optimized from earlier works. A single energy calculation was done in CP2K to determine the band position and bandgap of the listed ligands.

2.3. Adsorption and diffusion

Adsorption and diffusion properties have been investigated using RASPA software [36]. Adsorption computations were carried out in the grand canonical Monte Carlo simulations (GCMC), whereas diffusion coefficients were determined in the canonical ensemble. MOFs were simulated as rigid frameworks, where Lennard-Jones (LJ) potential parameters gather from the universal force field (UFF) [37]. Point charges are found using DFT and equilibration as implemented in RASPA. Nitrogen [38], oxygen [39], and ammonia with a 5-site model [40] were modeled using Transferable Potentials for Phase Equilibria (TraPPE) force field parameters. The TraPPE force field for ammonia has been used to measure properties (solubility and other thermochemical properties) [41–43] and adsorption on some nanostructures (MOFs and graphite) [44–49]. Water has been modeled using the TIP5P molecular model to obtain better geometry to reflect precise radial distribution function (RDF) plots [50]. Nonbonded interactions are modeled using LJ 12–6 with a spherical truncation at 12.8 Å while implementing tail correction. Standard Lorentz-Berthelot combining rules are used for unlike atoms LJ interactions.

2.4. Structural, geometrical and mechanical properties

Structural and related geometrical properties were found using open-source zeo++ code [51] and RASPA. Properties include largest cavity diameter (LCD), pore limiting diameter (LPD), accessible surface area, and volume and helium void fraction. We also used RDF to observe substrate in molecular simulations carried out in this study. All mechanical robustness indicators (bulk, shear, and Young's moduli) have been determined through the implementation of constant strain molecular mechanics in the Forcite module of Materials Studio [52] using universal force field (UFF) [37]. The above is the use of classical force field zero Kelvin elastic constants. Higher elastic moduli are desired as they correspond to the better mechanical stability of the structure. In this work, UFF has been used to describe interactions in the MOF since it has been shown to obtain an acceptable approximation of bulk moduli for several MOFs and comparable to DFT-based computations (IRMOF-1 and −10, HKUST-1, UiO-66) [53]. The application is assumed to occur at 1 bar, so the shear-mode softening effect is negligible [54].

2.5. Thermodynamic, energetic, and water stability

Although the materials screened in this work have been synthesized, we evaluate them in terms of their thermodynamic stability for comparison and place criteria for future MOFs discovery. The use of the heat of formation to guide screening purposes has been shown in screening perovskites for thermochemical water splitting reaction [55]. Here, the heat of formation is calculated as the difference between single point DFT calculation of the structure and individual constitutes (metal node and organic linker) to reflect MOFs' thermodynamic stability.

Water stability is an important parameter, especially in the photofixation of nitrogen, as water acts as the hydrogen source. Evaluating the response of a MOF's structure to the presence of water is intriguing. Chemical stability has been measured experimentally via Powder X-Ray Diffraction (PXRD) analysis, helium void fraction, and surface area (adsorption isotherm). Porosity should reflect partial degradation inapparent from PXRD analysis [56,57]. In this work, water adsorption in the studied MOFs is computed using GCMC simulations at room temperature and pressure. The final step of atomic configuration is transferred to DFT-based calculation, where zero temperature cell optimization is implemented to study the MOF's response. The cell optimization option available in CP2K allows cell parameters to fluctuate besides atomic coordinates as local energy minima are located. The optimized cell is then studied from the structural point of view by plotting PXRD and compared to the initial MOF before water adsorption. Besides, porosity and surface area are also monitored to explain structural differences. We also calculated the thermodynamic stability of MOF by estimating the free energy of the hydrolysis reaction and evaluating it.

2.6. Life cycle assessment

Life cycle assessment (LCA) is a systematic tool used to quantify an environmental load of materials. The results are used to initially screen materials using the metal node of the MOFs. Five selected impact categories are global warming potential, energy demand, acidification, freshwater eutrophication, and human toxicity. Inventory data were gathered from Nuss and Eckelman [58] alongside an equation obtained from Mohamed et al. [18] to normalize categories impact. The equation combines all five categories into one factor that calculates values relative to the maximum value in each category from the first-raw transition metals. It is important to note that this equation demonstrates equal distribution and importance of all selected impact categories.

Detailed cradle-to-gate LCA is carried out for the targeted MOFs to compare them, find alternatives, and provide new routes to synthesis. The MOFs are synthesized based on current and available synthesis routes on a laboratory scale. The study is performed in GaBi software [59], and the selected impact assessment methodology is ReCiPe; and this particular comparison, all impact categories are considered. The functional unit is 1 g of MOF material.

3. Results and discussion

The dataset has 13 different metals Cd, Co, Cr, Cu, Fe, Mn, Ni, Pd, Ru, Sc, Ti, V, Zn, and Na and Mg for framework charge balance and easing the equilibration process. Some metal cluster contains chloride and iodide, whereas some organic matter has sulfur content in it. Several ligands are used in this dataset; BTDD ($BTDD^{-2}$: bis(1H-1,2,3-triazolo [4,5-b],[4′,5′-i])dibenzo[1,4]dioxin), BBTA ($BBTA^{2-}$ = 1H,5H-benzo (1,2-d:4,5-d′)bistriazole), BTT (BTT^{3-} = 1,3,5-tris(1H-1,2,3-triazol-5-yl) benzene), BTP (BTP^{3-} = 1,3,5-tri(1H-pyrazol-4-yl)benzene), DOBDC ($DOBDC^{4-}$ = 2,5-dioxido,1,4-benzenedicarboxylate), mDOBDC ($mDOBDC^{4-}$ = 4,6-dioxido-1,3-benzenedicarboxylate), DSBDC ($DSBDC^{4-}$ = 2,5-disulfidobenzene-1,4,-dicarboxylate), BTC (BTC^{-3} = 1,3,5-benzenetricarboxylate), and other structures [19]. Table S2 lists the MOFs in the database and their chemical composition.

The variability in the dataset has been evaluated by checking the number of times metal is represented (Figure S2). From Figure S2, one can observe that Zn and Fe are leading the metals. It is worth mentioning that the database contains several structures that use Zn in mixed metal structures (MOF-5). From another perspective, pore limiting diameter, surface area, and void fraction of the MOFs are determined and reported in bar charts (Figure S3(a–c)). Although fewer structures than the HMOF database, the dataset is diverse in metal represented and surface area spanned. All structures have open metal sites, crucial for the catalytic application and thus viable for single-atom heterogeneous catalysis activity.

It is essential to highlight that the materials in this database are not comprehensive. In other words, some structures have not been synthesized based on all possible transition metals. Here, we expect the computational design to guide discovering new materials. To investigate more structures, CoRE MOFs were screened following geometrical screening processes (step 1–3 in Figure S4), which included surface area, limiting porosity, and availability of metal sites; 5768 MOFs were screened from the database. This number is much higher than HMOF or the 60 MOFs dataset. As a result of the large number, we introduced a Life Cycle Assessment (LCA)/abundance parameter that highlighted the use of Fe, Mn, Cr, and mixed metal MOFs containing a combination of the three metals. A total of 330 MOFs are left in the pool. Here, only Fe-based MOFs were electronically investigated as Fe is currently being tested for its photoactivity and possibility for integration in the nitrogen photofixation process, as discussed in the introduction section. Figure S5

summarizes the LCA main categories considered for evaluating first-raw transition metals. The structures obtained from the small dataset and those selected from CoRE make up the databases for the following analyses.

3.1. Electronic parameters

Here, the structures were studied using PBE and HSE06 functional for comparison and modeling purposes. Also, it is worth mentioning that the material's photoactivity region is altered here due to considering water, instead of hydrogen, as a raw material. Four structures satisfied the band edges' criterion; Fe_2Cl_2(BBTA), Ni-BTP, Fe_2(mDOBDC) and Zn_2(mDOBDC); however, only Fe_2Cl_2(BBTA) has a bandgap below 3.00 eV. Fig. 2 shows the structure of the four MOFs and the corresponding organic linker building block. In comparison, 14 structures can be marked for water splitting application. Some candidates include Mo-BTC, Cr-BTC, and Ni_2(DOBDC). For the photofixation of nitrogen, other potential MOFs include, Fe_2(DOBDC), Fe_2(DSBDC), and Mo-BTC. The latter three structures' inclusion is possible since other MOFs with similar properties have shown activity towards the photofixation process and open the possibility to inaccuracy in hybrid functional DFT computations. Also, the conduction band edge position can be altered due to the pathway and mechanistic nature present in a particular catalyst [60]. Fig. 3 shows the band energy plots for the four structures that have the potential for photofixation of nitrogen using water and molecular nitrogen. In contrast, Fig. 4 targets structures with appropriate band edges for water splitting reaction. Mo-BTC, Fe_2(DSBDC), and Ni_2(DOBDC) showed desired electronic properties for the water-splitting

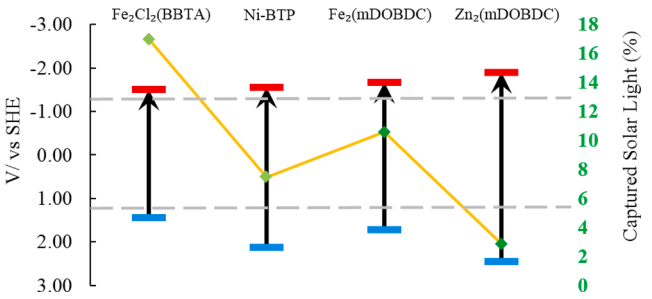

Fig. 3. Band energy plot of the four selected structures in the dataset using HSE06. Valence band (blue), conduction band (red), green points show the predicted captured solar light.

reactions.

The preliminary results from Fe-based MOFs from the CoRE MOFs database show Fe_2(DOBDC) as a potential material for performance testing using different obtained experimental structures. This MOF has been part of the Rosen et al. small dataset [19]. Another potential linker is DEBDC ($DOBDC^{4-}$ = 2,5-dihydroxybenzene-1,4-dicarboxylate), tested for electrical conductivity enhancement by Sun et al. [61]. There is a high potential of Fe-based MOF for water splitting reaction, while a high number can be used as part of Z-scheme-based catalysis. Castelli et al. utilized computational tools to screen perovskite metal oxides for photoelectrochemical cell application [62]. The concentration of the work was to search for stable materials with optimal, well-positioned band gaps. The work has been expanded to consider Z-scheme water splitting

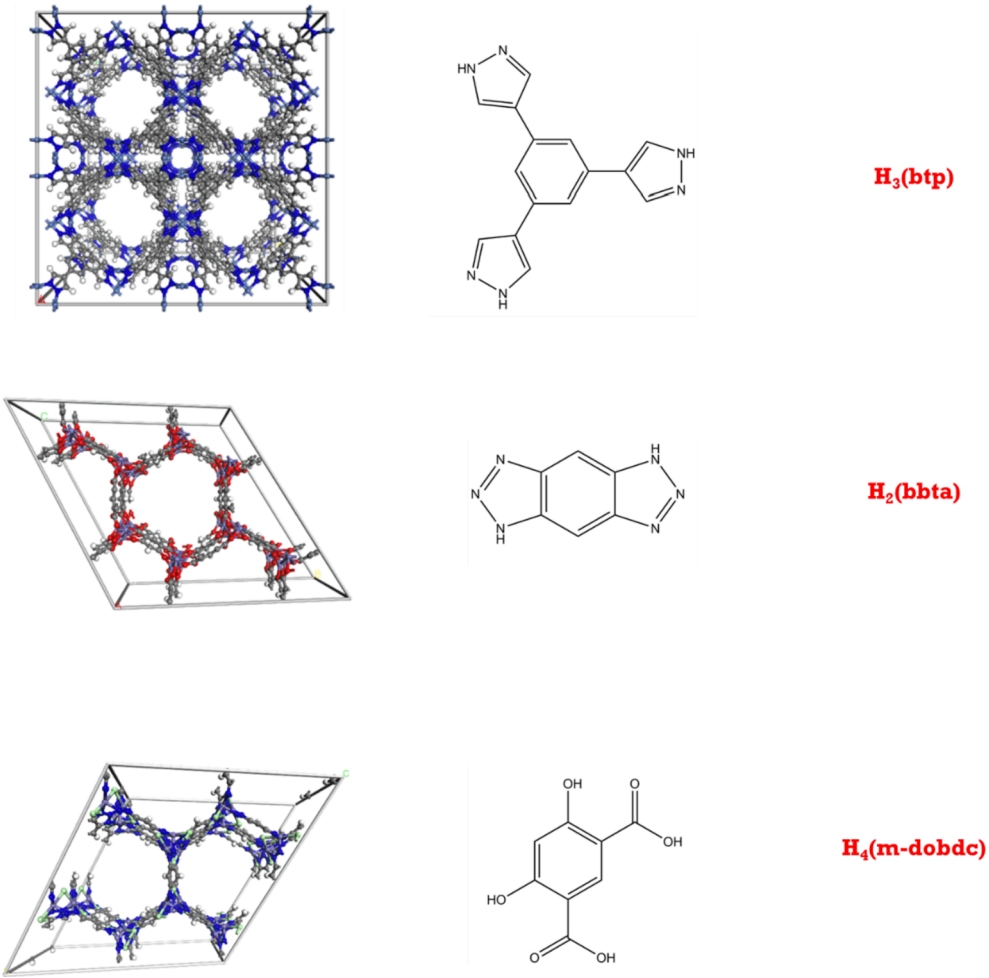

Fig. 2. Structure, organic linker, and its name for the selected four MOFs; BTP (Ni), BBTA (Fe), and mDOBDC (Fe and Zn).

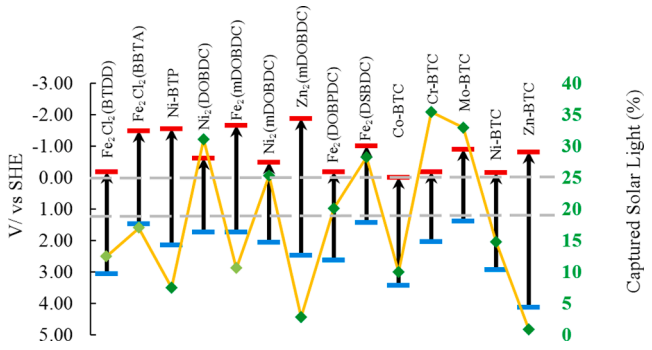

Fig. 4. Band energy plot of MOFs for water splitting reaction in the dataset using HSE06. Valence band (blue), conduction band (red), green points show the predicted captured solar light.

[63]. The paper listed the screening of perovskite towards one-photon and Tandem Cell schemes; and transparent shield application. In 2015, Castelli et al. managed to obtain five candidate materials for the one-photon water splitting photoelectrochemical device from the Materials Project Database [64]. Recently, Stylianou and coworkers demonstrated that appropriate alignment of MOF-MOF heterojunction increases charge separation efficiency [65]. MIL-167/MIL-125-NH_2 heterojunction improved the hydrogen production approximately nine folds pristine MIL-125-NH_2 [65].

Throughout the DFT screening of MOFs' experimental databases, several MOFs combinations can be seen as potential for highly efficient separation of charge carriers using semiconductor/semiconductor Z-scheme. Z-scheme ensures an extended lifetime of charge carriers and reduces the recombination rate because reduction and oxidation are in different materials [66]. We can extract a combination of structures from our computational results to satisfy electronic properties for the reaction utilizing direct Z-scheme photocatalysts [67]. Examples include binary photocatalytic combinations of the four structures with Fe_2Cl_2(BTDD), Ni_2Cl_2(BTDD), Ni_2(DOBDC), Ni_2(mDOBDC), Fe_2(DOBPDC), Mn_2(DOBPDC), Ni_2(DOBPDC), Co-BTC, Cr-BTC, Mo-BTC, Ni-BTC and Zn-BTC (Fig. 5). Combining the four selected materials shows type I heterojunction semiconductors that still provide better charge separation.

Not only can Z-scheme provide enhanced stability and high redox abilities, but it also allows to combine materials that have smaller bandgaps to absorb light in the infrared light region. Lower bandgap structures correlate well with improved photoexcitation as it takes less time for the electron to arrive at the conduction band. Near-infrared (NIR) region is between 780 and 1400 nm, corresponding to 1.58 to 0.886 eV. A combination theoretically projected to result in a higher ammonia efficiency is Mn_2(DOBPDC)/Ni_2Cl_2(BBTA)/phenyl-Zn-HKUST-1 bandgaps are 1.02, 1.85, and 2.4 eV, illustrated in Fig. 6. Mn-based MOFs have the lowest bandgaps among the investigated MOFs, where Mn_2(DOBPDC) can capture more than 80% of the energy content of the solar spectrum (up to 1200 nm). As Mn_2(DOBPDC) has a

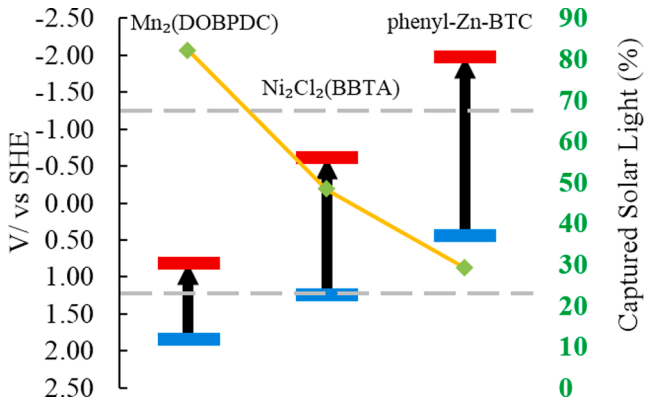

Fig. 6. Band energy plot of three MOFs for potential heterojunction direct Z-scheme, green points show the predicted captured solar light.

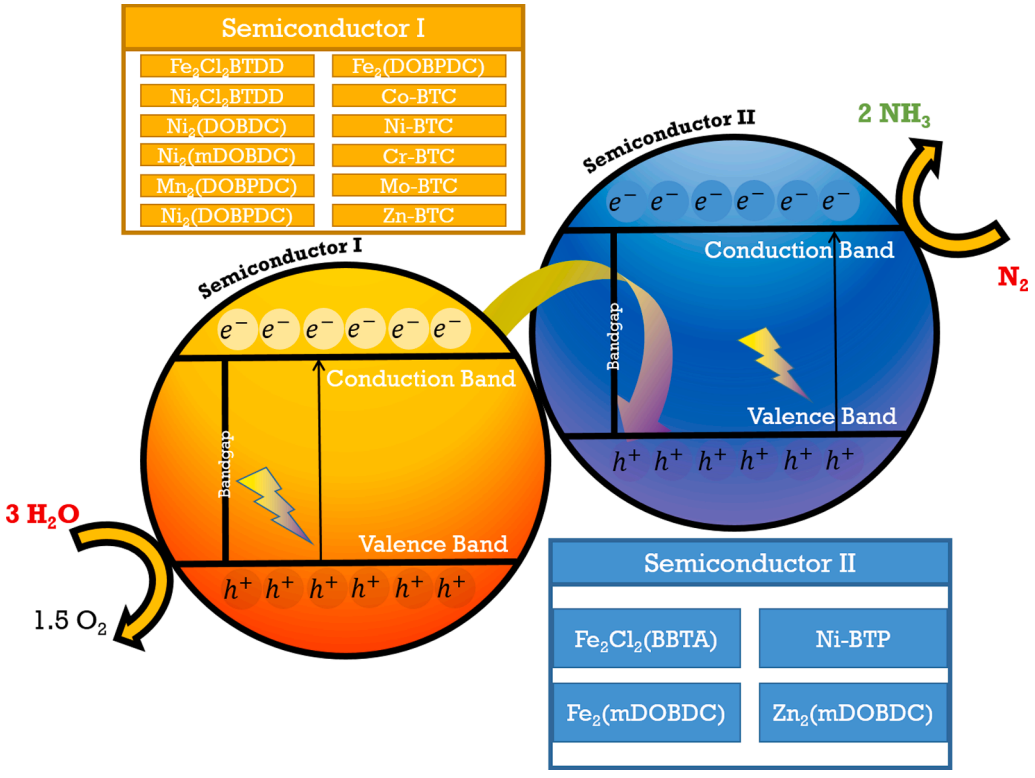

Fig. 5. Schematic diagram of direct Z-scheme heterojunction MOF based nitrogen photofixation process with proposed MOFs for semiconductor I and II.

considerably small bandgap, the relative ratio of charge carriers' masses is calculated to reflect the recombination rate. Mn_2(DOBPDC) has an average *D* parameter of 2.3, and the maximum is 5.4 in the Γ→*Z* path. As shown previously, ligand functionality is valuable for designing such sensitive materials for this specific application.

The density of state plots assists and indicates material capability regarding charge carrier separation and resistance to recombination, which is primarily responsible for low photocatalysis activity. The four materials reveal n-type semiconductor nature given the Fermi level's position relative to valence and conduction bands as reflected by DOS plots in Fig. 7. Here, the DOS plots are utilized to compare the four materials in terms of the density between the conduction band and the Fermi level. Higher density demonstrates the potential to capture conduction band electrons and increase the lifetime of the excited electron. In other words, higher density in that region increases the number of levels to accept an electron from the conduction band. Reflecting on the figure obtained, we conclude that Fe_2(mDOBDC) based MOFs have higher densities in that region.

Another take from state plots' density is to support potential mechanisms concerning the charge separation following the excitation stage. In Zn_2(mDOBDC), ligand to ligand is interpreted from DOS, whereas linker to metal can be associated with Ni-BTP. Fe_2Cl_2(BBTA) shows some combination of metal–metal, metal-linker, and linker-metal provided from the DOS plots. The metal contributes to Fe_2(mDOBDC)'s lowest unoccupied molecular orbital (LUMO) and HOMO levels. Given the predicted ligand to metal, we expect Ni-BTP and Fe_2Cl_2(BBTA) have longer-lived photogenerated charges due to spatial separation relative to Fe_2(mDOBDC) and Zn_2(mDOBDC) [33]. We can also note that higher levels (LUMO +) of Ni-BTP are highly dominated by states other than the metal; therefore, high energetic photonic absorption does possess similar properties. The analysis focuses on HOMO-LUMO levels after the high-energy photonic excitation relaxation process. It is important to note that an additional computational charge carrier mobility reflected by the charge carriers' mass is necessary to investigate experimental observation further. Here, as discussed in the methodological section of this paper, we introduce the relative charge carrier's mass as an indication of charge mobility. Table S3 summarizes the results associated with the examined MOFs. It can be concluded that Zn_2(mDOBDC) offers better charge separation relative to Fe_2(mDOBDC) and Fe_2Cl_2(BBTA), considering the relative effect masses of charge carriers. The DOS results indicated that Zn_2(mDOBDC) possesses ligand-centered spatial separation of charge carriers, characterized by short-lived charge carriers. For that reason, both spatial separation and relative effective mass have to be incorporated in the analysis. Heterojunction combinations can provide the necessary assistance in charge separation. It has to be noted that the studied MOFs are unfunctionalized in terms of additions to the organic linker. The addition of some functional groups can result in more desired charge masses.

In addition to the electronic properties, the number of active sites (metal atoms) per volume of the MOF has been calculated to determine which of the selected MOFs characterizes the highest active site density. The calculated figures are 4.50, 4.48, 4.08, and 1.88 sites/nm^3 for

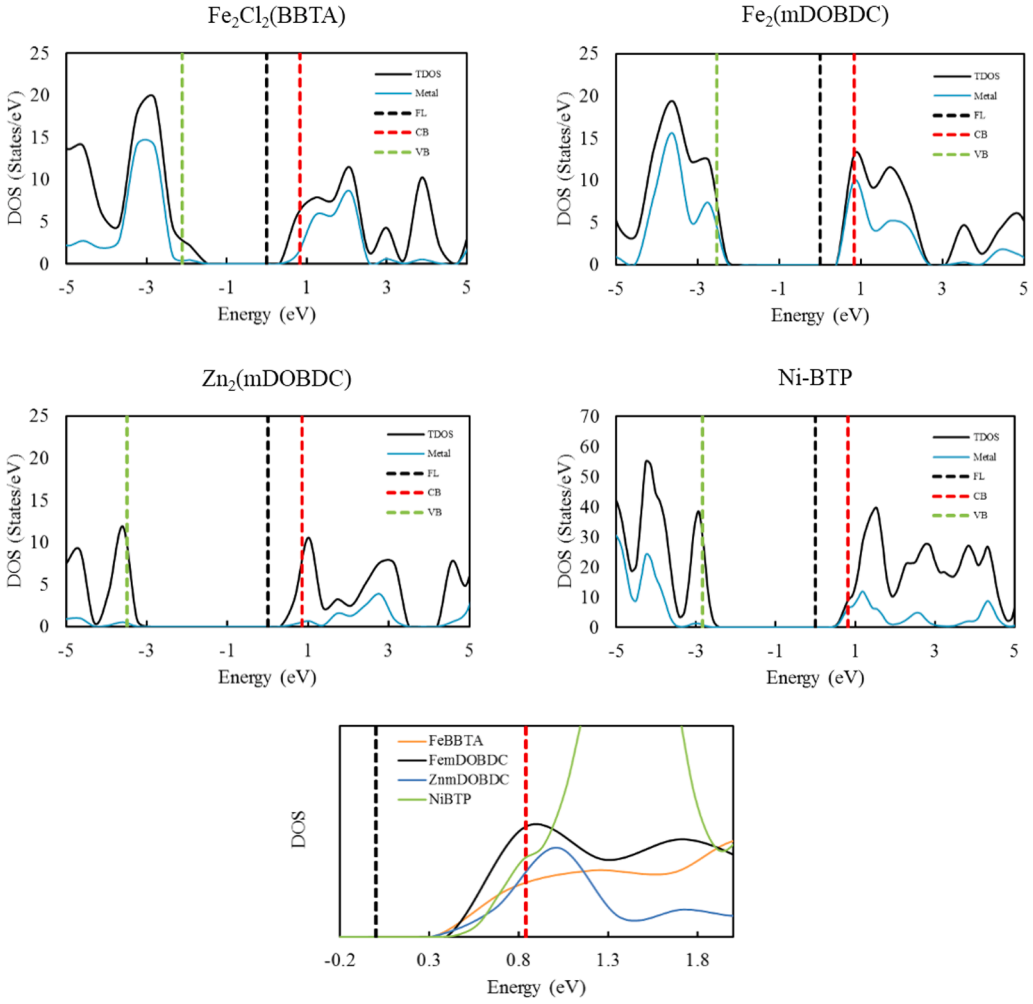

Fig. 7. The density of states (DOS) for the four selected MOFs, FL: Fermi Level (0 eV in the plots), CB: Conduction Band, VB: Valence Band, Metal, indicate the contribution from the metal element in the respective MOF using HSE06 functional. The oxidation state of metals is 2+, and the spin state of metals is low spin.

Fe_2(mDOBDC), Zn_2(mDOBDC), Fe_2Cl_2(BBTA), and Ni-BTP. A higher site density for mDOBDC based MOFs indicates the availability of multiple catalytic sites in proximity which is highly desired, especially in multiple components and protonation steps are associated with the desired reaction.

3.2. Adsorption and diffusion parameters

Transport phenomena simulations have to be accompanied to reveal adsorption favored locations and energies of the involved species. The duration of the light absorption photophysical process and electron transition from HOMO to LUMO is in the order of femtoseconds. Thus the presence of reactants, mainly nitrogen diatomic, in the active site proximity is necessary to avoid the formation of undesired reaction or inactivity towards the fixation process. Hydrogen evolution has to be avoided to increase selectivity towards ammonia synthesis.

Adsorption parameters have been quantified for the case of ammonia and water to especially evaluate adsorption and heat of adsorption values, as shown in Figure S4 and Figure S5. The results presented in Figures S6 and S7 are concerned with the dataset of 60 MOFs. Although the choice of force field impacts gas separation performance evaluation, Dokur and Keskin showed that MOFs' ranking using metrics is not sensitive [68,69]. The highest occurrence of ammonia's adsorption is approximately 1 mol/kg with 25 structures; however, three structures exceeded the 6 mol/kg mark. Ammonia isosteric heat of adsorption values ranges between 10.8 and 30.3 kJ/mol. The 19.1 kJ/mol bin contains the highest frequency with 16 structures. A single structure exceeded the 28 kJ/mol threshold.

On the other hand, the average heat of adsorption of water values was relatively higher than ammonia. The structures have absolute heat of adsorption values higher than 40 kJ/mol except a few. A higher than 40 kJ/mol value reflects the strong interactions between the structure and water, mostly related to the open site metal and water electronic properties. Generic force fields such as UFF typically do not fully describe MOFs' interaction with OMS and adsorbates.

One must ensure that nitrogen molecules can reach the active site for the fixation reaction. We computed the adsorption of nitrogen and diffusion-based simulation using MD of nitrogen, water, and oxygen in the pure component from a computational perspective. In high water loading in the MOF, it is necessary to comprehend such systems' dynamic behavior. Detailed adsorption results at 1 bar and 298 K, Henry's constants, the heat of adsorption, and self-diffusion coefficients can be found in the supporting information (SI) document.

Nitrogen adsorption Henry's constant per number of the active sites is comparable between the four materials except for Ni-BTP, as shown in Table 1. However, the adsorption location reflected by the RDF of the nitrogen atom shows that the nitrogen molecule is closest to the metal in Fe_2(mDOBDC). The proximity of the nitrogen dimer to the metal node is affected by the metal-linker complex's angle. It be can be noted from the RDF comparison between the four structures that mDOBDC structure MOFs exhibit higher probability before the first peak (Figure S8).

The ideal adsorption selectivities, obtained from Henry's constants ratios, were calculated for N_2/NH_3 and H_2O/NH_3 pairs to reflect adsorption and desorption of reactants and products, respectively. Ideal selectivities are reported in Table 1; self-diffusivity and single gas permeability can be found in Table S4. Ideal adsorption H_2O/NH_3 selectivities alongside permeabilities ratios proved that Fe_2Cl_2(BBTA) and Fe_2(mDOBDC) are selective towards water instead of ammonia. The same cannot be concluded for the other two MOFs. We supported this outcome with NVT-MD simulations of water and ammonia equimolar fluid composition, where diffusion coefficients and RDF are reported in the SI document (Figure S9 and Table S5). The heat of ammonia adsorption in Ni-BTP is −25 kJ/mol higher than the three other materials relative to the −16 to −17 kJ/mol. The difference between the heat of water adsorption and ammonia ta 1 bar and 298 K is highest in Fe_2(mDOBDC), which is essential to reflect H_2O/NH_3 adsorption. As expected, nitrogen adsorption is considered very low relative to water adsorption.

Examining oxygen is critical since utilizing an air mixture instead of a pure nitrogen stream would make the overall system more cost-effective. The presence of oxygen in the nitrogen stream is detrimental to the fixation process. Oxygen molecule leads to nitrate and nitrite formation, which are undesired in this process and directly impact selectivity and activity [70]. Although one can argue that oxygen can act as an electron sink and thus reduce the energy carrier recombination losses, a study showed that oxygen hindered nitrogen reduction by trapping some photogenerated electrons [71]. Recent research targets electrocatalytic conversion of nitrate to ammonia [72], so subsequent conversion to ammonia can be targeted. Further research in the field of nitrate conversion to ammonia has to be conducted.

In this work, Henry's constant adsorption ratio and co-adsorption of air mixture molecules at 1 bar and 298 K have been carried out to study MOFs' preferential adsorption. Corresponding results of this section can also be found in Table 1. The four MOFs are slightly oxygen favorable; however, at the dry air composition (79%:21%, N_2:O_2), oxygen is present mainly in the middle of the MOF's cavity, with excess adsorption selectivity up to 10 fold higher than ideal selectivities. We also note that Ni-BTP does not show similar behavior as the other three MOFs in increased selectivity between absolute and excess adsorption. Also, simulation of water-saturated MOFs with air mixture has been investigated to study the RDF after equilibration (mole fraction: 75.6, 19.5, 4.9% for H_2O, N_2, O_2). A comparison of water and nitrogen RDFs with the metal has been made to the case of oxygen presence (Figure S10).

We can conclude from this study that oxygen absence is necessary as the studied MOFs do not present preferential adsorption of nitrogen. Suggestions from the diffusion and adsorption studies maintain the possibility of inactive nitrogen regions of the MOF. However, special experimental measurements must be taken to overcome low nitrogen solubilities in the water at room temperature. These results confirm that experiments should avoid air when assessing MOFs' nitrogen fixation capabilities. Removal of oxygen can be accomplished by purging nitrogen gas (batch and flow), preparing catalysts in a nitrogen atmosphere (glovebox), or removing oxygen using chemicals such as salts.

Table 1
List of relevant adsorption properties of MOFs (selectivities and RDF).

MOF	$K^0_{N_2}$	$\frac{K^0_{N_2}}{K^0_{NH_3}}$	$\frac{K^0_{H_2O}}{K^0_{NH_3}}$	RDF nearest position	$\frac{K^0_{N_2}}{K^0_{O_2}}$	Adsorption selectivity at dry air condition $\frac{N^0_{N_2}}{N^0_{O_2}}$	
						Absolute adsorption	**Excess adsorption**
	mol/mol(M)/bar	**mol/mol**	**mol/mol**	Å	**mol/mol**	**mol/mol**	**mol/mol**
Fe_2Cl_2(BBTA)	0.039	0.077	2.141	2.364	0.946	3.57	9.40
Ni-BTP	0.135	0.143	0.319	2.484	0.916	3.43	4.61
Fe_2(mDOBDC)	0.033	0.038	2.071	2.340	0.973	3.63	10.25
Zn_2(mDOBDC)	0.036	0.201	0.204	2.412	0.929	3.48	9.32

3.3. Mechanical stability

Although MOFs' application in photocatalysis of nitrogen reduction is immature, our investigation of elastic properties provides essential information regarding structural stability and materials' stiffness. Candidate materials are expected to maintain their porosity and structure during practical application processes, such as pelletization and extrusion [73]. We introduced the mechanical properties calculations because special attention has to be paid towards MOFs with high porosity (greater than 0.4) [74].

In this work, several mechanical indicators are used, which are the bulk modulus is denoted by *K,* and shear modulus is denoted by *G* [74]. Bulk modulus is the inverse of compressibility, whereas the shear modulus is the rigidity modulus. Young's modulus provides information about the compressive stiffness of a material. As expected, elastic and bulk moduli are higher than shear moduli for the case of MOFs. The results show that the most suitable MOFs is Fe_2(mDOBDC) as it has a shear modulus in the 30 GPa range while having a bulk modulus higher than 40 GPa (~50GPa); besides being the stiffest among the shortlisted candidates. The reported elastic constants are in the range of pure inorganic porous nano-frameworks such as zeolites (20–120 GPa) [74]. Compared to Zn_2(mDOBDC), Fe_2(mDOBDC) has improved mechanical properties (Young's, bulk, and shear moduli), which can be attributed to higher bond strength between the linker terminal and the Fe atom. Ni-BTA, Fe_2(mDOBDC), and Zn_2(mDOBDC) have 16, 20, and 22 GPa in shear modulus, respectively. These values are comparable to UiO66 in the absolute shear modulus [74]. Although UiO66 has a high coordination number, it has been shown that Fe_2(mDOBDC) has approximately double the mechanical properties values. This rather illustrates the organic linker effect besides the coordination number of the MOF, as also noted in the literature [75]. The study by Banlusan and Strachan supports the ability to tune mechanical properties through organic linker selection [75].

The maximum lengths of the organic linkers' connection points are reported in Table 2 alongside structures' void fractions. Fe- and Zn-based mDOBDC has an equivalent void fraction; however, the difference in stiffness is apparent mainly due to the stronger bind between Fe—N. The results confirm that higher linker length (and thus void fraction) leads to lower mechanical properties, as demonstrated by the Ni-BTP case.

3.4. Thermal and chemical stability

From the DFT computations' energetic stability point of view, Fe_2(mDOBDC) and Fe_2Cl_2(BBTA) are the top two among the four studied MOFs at −589.2 and −562.1 eV/atom, respectively. Thermal stability can be seen as a combination of organic–inorganic bond strength (node-linker) and the number of organic linkers attached to the node [56]. We can note that the energetic stability is essentially correlated well with the studied materials' mechanical properties. Thermal and hydrothermal stabilities are essential in MOFs, but water resistance is highly relevant for applications of photofixation at low temperatures and pressures.

Potential MOFs should tolerate pH between 5.5 and 11 between pure distilled water and ammonia. Using cell optimization procedure implemented in CP2K, water chemical stability has been studied following water adsorption at 1 bar and 298 K (output from GCMC). The energy difference is calculated as the difference between energy after adsorption of water minus individual MOF and water molecules as a form of thermodynamic stability. Although free energy needs to be computed coupled with the kinetic barrier to understand MOF's behavior fully, the electronic energy at zero Kelvin provides critical information, especially at adsorption of water in the cavity of the MOFs. The results show that the Ni-BTP and Zn_2(mDOBDC) have better stability than Fe_2Cl_2(BBTA) and Fe_2(mDOBDC), where Fe_2(mDOBDC) has the lower water stability among the list (Table S6). We studied the water chemical stability of Fe_2(mDOBDC), Zn_2(mDOBDC), and Fe_2Cl_2(BBTA), where Ni-BTP can be seen as a benchmark as it has been revealed experimentally to be stable in a vast range of boiling aqueous solutions acidity [76]. In the case of Fe_2Cl_2(BBTA), we observe a shift in the first peak of the PXRD (Figure S11); the reason behind the shift can be understood by the increase of cell volume (5.75% increase) and slight deformation as a result of an increase in the Fe-Cl-Fe angle.

3.5. Life cycle assessment

A detailed cradle-to-gate LCA has been carried out in this work. Information about the synthesis route selected for the inventory analysis can be found in the supporting document (Table S7-S9 and text concerning the steps associated with MOFs synthesis). The overall environmental impact comparison between the four MOFs using 15 different impact categories showed that the environmental burden ranking is as follows; Fe_2Cl_2(BBTA) > Zn_2(mDOBDC) > Fe_2(mDOBDC) > Ni-BTP. Figure S12 depicts a quantitative comparison in two specific categories: climate change and human toxicity. We can calculate that producing a gram of Fe_2Cl_2(BBTA), Zn_2(mDOBDC), Fe_2(mDOBDC), and Ni-BTP results of 2.19, 1.49, 1.33, and 0.35 kg CO_2 (eq.), respectively. Meanwhile, Fe_2Cl_2(BBTA) has 2.4 folds the impact from the other MOFs in the human toxicity category. The contribution analysis concludes that most of the environmental impact is due to chemical solvents utilized in the processes. Fe_2Cl_2(BBTA) has the most chemical steps, as shown in Table S9, which entails additional solvent consumptions. Implementing ideas such as using waste plastic to produce MOFs [77] and eliminating chemical solvents in MOF preparation will reduce the overall environmental impact of MOFs.

3.6. Understanding the role of MOF's building unit on electronic properties

This work sets a target to understand the role of each of the MOF's building units (metal node or metal cluster, and organic ligand) on the electronic properties and subsequently on its selection for photocatalytic reactions. Comprehending the individual functionality should lead to a better design of MOFs by integrating engineering concepts. The organic linker can offer opportunities to tune bandgap due to the linker's total substitution, partial substitution, Metallo-, and the wide range of available organic functionalization. Ligands themselves may be characterized using the covalent bond classification (CBC) methods, indicating the number of electrons donated or accepted by the ligands' metal. Whereas the metal has the effect of the node or cluster, metal

Table 2
Comparison between studied MOFs in the mechanical robustness (Bulk, Shear, and Young's moduli) and relevant structural properties.

MOF	Helium void fraction	Length of organic linker (Å)	Metal-O/N Coordination no.	Bulk Modulus (GPa)	Shear Modulus (GPa)	Young's Modulus (GPa)		
						X	Y	Z
Fe_2Cl_2(BBTA)	0.698	6.44	3	22.6	20.2	81.6	32.4	32.9
Ni-BTP	0.795	9.42	4	15.4	16.3	29.3	29.4	29.3
Fe_2(mDOBDC)	0.691	6.38	5	50.2	31.4	140.9	51.6	53.2
Zn_2(mDOBDC)	0.706	6.38	5	29.5	22.4	87.0	34.0	36.4

substitution and metal on Metallo-. Also, the role of topology and cluster models are yet to be discovered. What is sought is a relationship between components' bandgap and structure bandgap, in some manner, similar to the relationship between composition and bandgap delivered by the empirical finding in Vegard's combination law. The main objective is to provide a predictive model of bandgap and edges using DFT calculations.

3.6.1. Metal center

Several attempts have not been successfully correlated bandgaps with the properties of solids or constituent elements in the solid [78]. Failure to construct an empirical correlation has been attributed to the limited number of data points used to derive correlations.

$$BG_{structure} = -CE_{free} + BG_{linker} \quad (3)$$

Fig. 8 shows an attempt to understand the metal's role in determining the structure's electronic properties. It uses the maximum number of electrons that the metal can lose to reach the partially or filled d-orbital from the metal center's outer electronic shell oxidation state. The available electrons count is plotted versus the bandgap of M−BTC and M_2(mDOBDC) MOFs. A particular case is Mn^{2+}, as we assigned 5 electrons for the cation. In these MOFs families, the metals are in a 2+ oxidation state. A linear relationship shows a high correlation between the two properties while fixing the y-axis intercept at the organic linker bandgap (BTC). A novel correlation can be deduced from this relationship as follows:

The slope *C* could potentially illustrate the importance of the structure and morphology of the MOF in its electronic properties. A negative gradient as a function of the number of electrons illustrates the bandgap reduction as it becomes easier to remove an extra electron of the metal cation. Further analysis and transferability are still in progress; however, this correlation can be one of the leading models to design a new set of MOFs for various environmental applications. The intercept is set to equal the linker's bandgap found from a separate DFT computation at the same theory level as structures' simulations.

The slope is more prominent in the case of mDOBDC, which indicates that in these MOFs, bandgaps are more prone to metal electron counts. In the case of the BTC-based linker, at 3 electrons and 4 electrons, there are two metals in the list of structures studied. The bandgap decreases as one goes down a group in the periodic table, as the difference between energy decreases (bonds become weaker) as the principal quantum number increases. The difference is relatively insignificant between Cr and Mo (4 electrons). If we only consider metals from the third-row transition metals, the determination coefficient is approximately 0.985. We studied the MOFs' DOS to justify the correlation, emphasizing the metal center at the two crucial energy levels (HOMO and LUMO), Figure S13. The plots indicate that metal has little to no accessible levels in Zn-based MOFs. Other metal-based MOFs significantly contribute from d-orbital metal states, explaining the opportunity to isolate metal effect in the correlation. Generally, as shown in the figures, the metal has less of a portion of the total DOS in mDOBDC, which can be reflected from the lower value of determination relative to BTC linker MOFs in Figure S13.

Another property we investigated is the difference between ionization energies of the metal-centered atom as an indicator. The property measures the energy needed to pull an extra electron of the metal at the corresponding oxidation state. Fig. 9 successfully reveals the relationship between the conduction band edge of the MOF and the ionization energy difference value of several atom types. The determination's coefficient reached 99.3%, corresponding to a high correlation using a second-degree polynomial. Nevertheless, no attempts have been made to understand the reasoning behind this. Throughout the combination of the two correlations, important electronic properties for a particular photocatalysis can be collected to select materials. We believe that this is the first time MOFs' building blocks are used to estimate the MOFs' electronic properties.

3.6.2. Effect of the organic linker

The organic part of the MOF is essential as it contributes to the structure size, mechanical stability, thermal stability, and, most importantly, electronic properties. One of the ways that make them highly tunable is functionality. The role of functionalization has been studied previously in the literature. Some organic linker properties to consider when correlating are the energy of formation, dissociation temperature, electronic properties, length, number of coordination sites. This step aims to demonstrate the ability to estimate MOFs' bandgap and electronic properties from organic linkers.

Fig. 10 illustrates an attempt to correlate the ligand's bandgap to the structure's bandgap. The data points were used to reflect ligands' influence isolation separately using Fe, Mn, and Ni-based structures. Several functions have been attempted to model the trend, the relationship following a sinusoidal function ($a\sin(bx+c) + d$) exhibited the highest coefficient of determination. Table S10 lists the fitting parameters of the model alongside the coefficient of determination. We can observe that organic linker's influence is minimal in Mn's case while it has a higher contribution in Fe and Ni. Organic linker's bandgap can provide essential knowledge of the electronic structure properties. On the other hand, data compiled from HMOF's previous screening shows that the mixed ligand's effect is reflected by taking the ligands' mole ratio composition. Some essential literature on predictive modeling using DFT was demonstrated by Lee et al. [79]. The work demonstrated using machine learning techniques with DFT to build robust models for AX binary compounds [79].

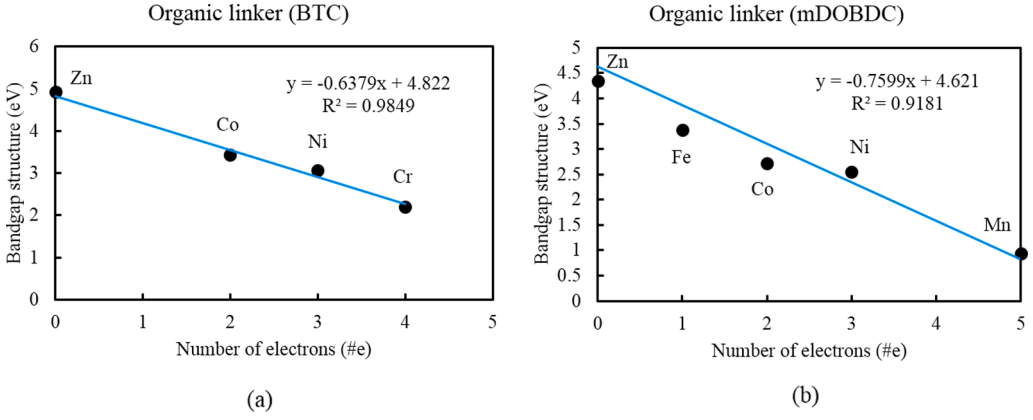

Fig. 8. The effect of the accessible number of electrons on the structure bandgap (a) BTC (b) mDOBDC (third raw transition metals).

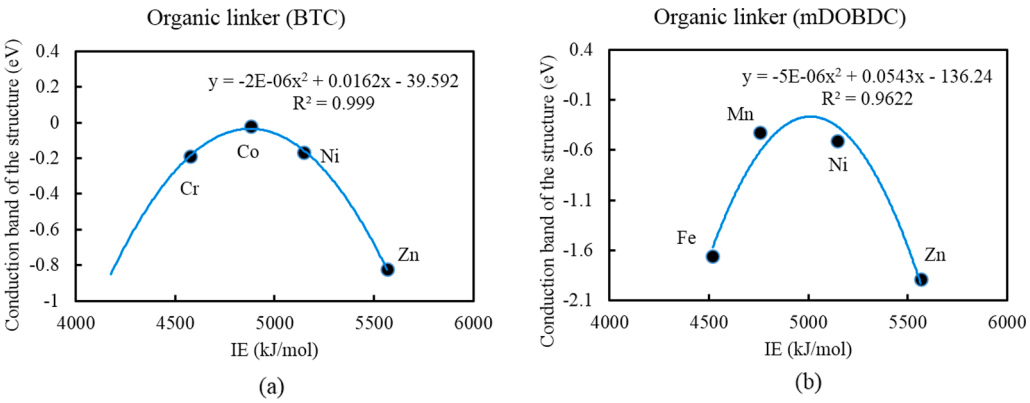

Fig. 9. The effect of the IE parameter on the structure conduction band (a) BTC (b) mDOBDC (third raw transition metals).

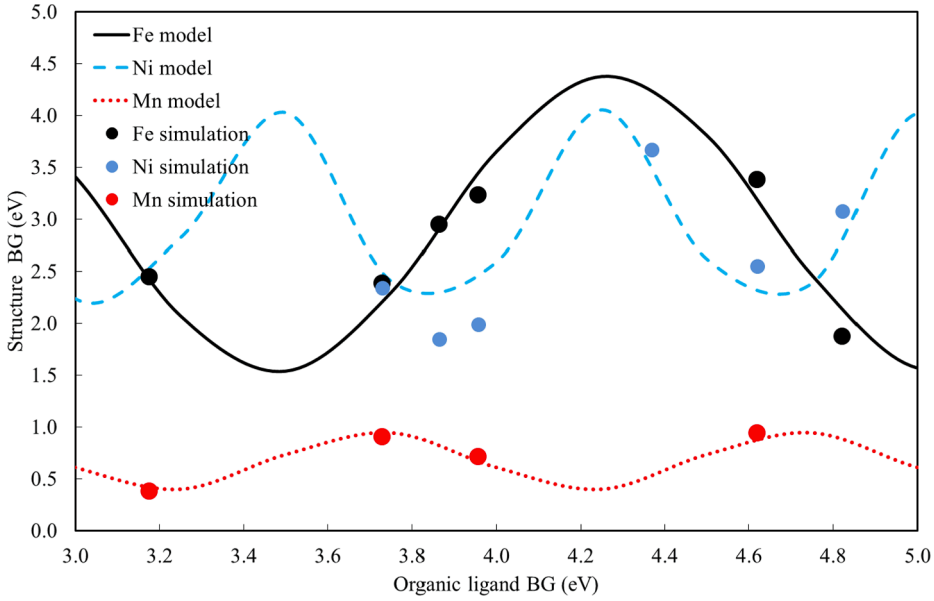

Fig. 10. The relationship between ligand and structure bandgaps in Fe, Ni, and Mn-based MOFs.

4. Conclusions

MOF chemistry allows for efficient use in numerous applications, predominantly adapting their characteristics to a particular desired application. This research effort utilized computational tools to screen and evaluate various MOFs for effective nitrogen photoreduction to ammonia. The photofixation application paves the minimization of environmental impact in current ammonia production. Computational techniques including DFT, molecular simulations, and geometrical analyzes were executed to analyze MOFs' electronic, adsorption, diffusion, structural and stability-related properties. Four MOFs were highlighted as potential candidates for the nitrogen fixation process, while several were nominated for water-splitting reactions from the examined material dataset. Analysis of the density of HOMO and LUMO levels shed light on the predicted form of charge transfer in the four structures.

Additionally, we proposed combinations of MOFs to assemble Z-scheme heterojunction-based photocatalysis to facilitate charge carrier mobility and minimize charge recombination. The selected four structures show reasonable shear modulus, and Fe_2(mDOBDC) revealed the best mechanical robustness among the four materials. Molecular transport properties showed the importance of maximizing nitrogen adsorption and the effect of oxygen in the diffusion and adsorption of reactants in MOFs. Also, we successfully constructed models to predict MOFs' bandgap and band edges from their building blocks (organic ligand and metal center) by studying the particular ligands and metal sites. This work's outcomes open the door towards efficient design and selection of MOFs for the photofixation of nitrogen and other photocatalysis activity. Some vital future research lies in determining the mechanism of nitrogen fixation in specific MOFs, which is essential to assist, modify and adjust structures for enhanced activity besides light absorption and thermodynamic driven parameters of the materials.

CRediT authorship contribution statement

Amro M.O. Mohamed: Conceptualization, Methodology, Formal analysis, Investigation, Resources, Data curation, Writing – original draft, Writing – review & editing, Funding acquisition. **Yusuf Bicer:** Supervision, Writing – review & editing.

Declaration of Competing Interest

The authors declare that they have no known competing financial interests or personal relationships that could have appeared to influence the work reported in this paper.

Acknowledgment

This publication was made possible by an Award GSRA5-1-0513-18051 from Qatar National Research Fund (a member of Qatar Foundation). We are grateful to the High Performance Computing Center of Texas A&M University at Qatar for generous resource allocation. Open Access funding provided by the Qatar National Library.

Data availability

The raw/processed data required to reproduce these findings cannot be shared at this time as the data also forms part of an ongoing study.

Appendix A. Supplementary material

Supplementary data to this article can be found online at https://doi.org/10.1016/j.apsusc.2021.152376.

References

[1] The Royal Society, Ammonia: zero-carbon fertiliser, fuel and energy store, London, 2020. http://royalsociety.org/green-ammonia.
[2] D.R. MacFarlane, P.V. Cherepanov, J. Choi, B.H.R. Suryanto, R.Y. Hodgetts, J. M. Bakker, F.M. Ferrero Vallana, A.N. Simonov, A Roadmap to the Ammonia Economy, Joule. 4 (2020) 1186–1205, https://doi.org/10.1016/j.joule.2020.04.00.
[3] P. Kumar, A. Deep, K.-H. Kim, Metal organic frameworks for sensing applications, TrAC, Trends Anal. Chem. 73 (2015) 39–53, https://doi.org/10.1016/j.trac.2015.04.009.
[4] K. Meyer, M. Ranocchiari, J.A. van Bokhoven, Metal organic frameworks for photocatalytic water splitting, Energy Environ. Sci. 8 (7) (2015) 1923–1937, https://doi.org/10.1039/C5EE00161G.
[5] R. Zhu, J. Ding, Y. Xu, J. Yang, Q. Xu, H. Pang, π-Conjugated Molecule Boosts Metal-Organic Frameworks as Efficient Oxygen Evolution Reaction Catalysts, Small. 14 (50) (2018) 1803576, https://doi.org/10.1002/smll.201803576.
[6] V.R. Bakuru, M.E. DMello, S.B. Kalidindi, Metal-Organic Frameworks for Hydrogen Energy Applications: Advances and Challenges, ChemPhysChem. 20 (10) (2019) 1177–1215, https://doi.org/10.1002/cphc.201801147.
[7] S.A. Younis, E.E. Kwon, M. Qasim, K.-H. Kim, T. Kim, D. Kukkar, X. Dou, I. Ali, Metal-organic framework as a photocatalyst: Progress in modulation strategies and environmental/energy applications, Prog. Energy Combust. Sci. 81 (2020) 100870, https://doi.org/10.1016/j.pecs.2020.100870.
[8] A.M. Al-Enizi, M. Ubaidullah, J. Ahmed, T. Ahamad, T. Ahmad, S.F. Shaikh, M. u. Naushad, Synthesis of NiOx@NPC composite for high-performance supercapacitor via waste PET plastic-derived Ni-MOF, Compos. Part B Eng. 183 (2020) 107655.
[9] R. Zhu, J. Ding, L. Jin, H. Pang, Interpenetrated structures appeared in supramolecular cages, MOFs, COFs, Coord. Chem. Rev. 389 (2019) 119–140, https://doi.org/10.1016/j.ccr.2019.03.002.
[10] H. Daglar, S. Keskin, Recent advances, opportunities, and challenges in high-throughput computational screening of MOFs for gas separations, Coord. Chem. Rev. 422 (2020) 213470, https://doi.org/10.1016/j.ccr.2020.213470.
[11] X. Chen, N. Li, Z. Kong, W.-J. Ong, X. Zhao, Photocatalytic fixation of nitrogen to ammonia: state-of-the-art advancements and future prospects, Mater. Horizons. 5 (1) (2018) 9–27, https://doi.org/10.1039/C7MH00557A.
[12] Y. Qian, F. Zhang, H. Pang, A Review of MOFs and Their Composites-Based Photocatalysts: Synthesis and Applications, Adv. Funct. Mater. 31 (37) (2021) 2104231, https://doi.org/10.1002/adfm.202104231.
[13] D. Li, H.-Q. Xu, L. Jiao, H.-L. Jiang, Metal-organic frameworks for catalysis: State of the art, challenges, and opportunities, EnergyChem. 1 (1) (2019) 100005, https://doi.org/10.1016/j.enchem.2019.100005.
[14] H. Huang, X.-S. Wang, D. Philo, F. Ichihara, H. Song, Y. Li, D. Li, T. Qiu, S. Wang, J. Ye, Toward visible-light-assisted photocatalytic nitrogen fixation: A titanium metal organic framework with functionalized ligands, Appl. Catal. B Environ. 267 (2020) 118686, https://doi.org/10.1016/j.apcatb.2020.118686.
[15] G. Li, F. Li, J. Liu, C. Fan, Fe-based MOFs for photocatalytic N2 reduction: Key role of transition metal iron in nitrogen activation, J. Solid State Chem. 285 (2020) 121245, https://doi.org/10.1016/j.jssc.2020.121245.
[16] Z. Zhao, D. Yang, H. Ren, K.e. An, Y. Chen, Z. Zhou, W. Wang, Z. Jiang, Nitrogenase-inspired mixed-valence MIL-53(FeII/FeIII) for photocatalytic nitrogen fixation, Chem. Eng. J. 400 (2020) 125929, https://doi.org/10.1016/j.cej.2020.125929.
[17] Z. Ding, S. Wang, X. Chang, D.-H. Wang, T. Zhang, Nano-MOF@defected film C 3 N 4 Z-scheme composite for visible-light photocatalytic nitrogen fixation, RSC Adv. 10 (44) (2020) 26246–26255, https://doi.org/10.1039/D0RA03562A.
[18] A.M.O. Mohamed, Y. Bicer, A comprehensive methodology to screen metal-organic frameworks towards sustainable photofixation of nitrogen, Comput. Chem. Eng. 144 (2021) 107130, https://doi.org/10.1016/j.compchemeng.2020.107130.
[19] A.S. Rosen, J.M. Notestein, R.Q. Snurr, Structure-activity relationships that identify metal-organic framework catalysts for methane activation, ACS Catal. 9 (4) (2019) 3576–3587, https://doi.org/10.1021/acscatal.8b05178.
[20] Y.G. Chung, E. Haldoupis, B.J. Bucior, M. Haranczyk, S. Lee, H. Zhang, K. D. Vogiatzis, M. Milisavljevic, S. Ling, J.S. Camp, B. Slater, J.I. Siepmann, D. S. Sholl, R.Q. Snurr, Advances, updates, and analytics for the computation-ready, experimental metal-organic framework database: CoRE MOF 2019, J. Chem. Eng. Data. 64 (12) (2019) 5985–5998, https://doi.org/10.1021/acs.jced.9b00835.
[21] Y.G. Chung, J. Camp, M. Haranczyk, B.J. Sikora, W. Bury, V. Krungleviciute, T. Yildirim, O.K. Farha, D.S. Sholl, R.Q. Snurr, Computation-Ready, Experimental Metal-Organic Frameworks: A Tool To Enable High-Throughput Screening of Nanoporous Crystals, Chem. Mater. 26 (21) (2014) 6185–6192, https://doi.org/10.1021/cm502594j.
[22] The CP2K developers group, (2008). http://www.cp2k.org.
[23] J. Hutter, M. Iannuzzi, F. Schiffmann, J. VandeVondele, CP2K: atomistic simulations of condensed matter systems, Wiley Interdiscip. Rev. Comput. Mol. Sci. 4 (2014) 15–25, https://doi.org/10.1002/wcms.1159.
[24] J.P. Perdew, K. Burke, M. Ernzerhof, Generalized Gradient Approximation Made Simple, Phys. Rev. Lett. 78 (1997) 1396, https://doi.org/10.1103/PhysRevLett.78.1396.
[25] A.V. Krukau, O.A. Vydrov, A.F. Izmaylov, G.E. Scuseria, Influence of the exchange screening parameter on the performance of screened hybrid functionals, J. Chem. Phys. 125 (22) (2006) 224106, https://doi.org/10.1063/1.2404663.
[26] M. Guidon, J. Hutter, J. VandeVondele, Auxiliary Density Matrix Methods for Hartree−Fock Exchange Calculations, J. Chem. Theory Comput. 6 (8) (2010) 2348–2364, https://doi.org/10.1021/ct1002225.
[27] S. Goedecker, M. Teter, J. Hutter, Separable dual-space Gaussian pseudopotentials, Phys. Rev. B. 54 (3) (1996) 1703–1710, https://doi.org/10.1103/PhysRevB.54.1703.
[28] C. Hartwigsen, S. Goedecker, J. Hutter, Relativistic separable dual-space Gaussian pseudopotentials from H to Rn, Phys. Rev. B. 58 (7) (1998) 3641–3662, https://doi.org/10.1103/PhysRevB.58.3641.
[29] J. VandeVondele, J. Hutter, Gaussian basis sets for accurate calculations on molecular systems in gas and condensed phases, J. Chem. Phys. 127 (11) (2007) 114105, https://doi.org/10.1063/1.2770708.
[30] X. Liu, J. Cheng, M. Sprik, Aqueous Transition-Metal Cations as Impurities in a Wide Gap Oxide: The Cu 2+ /Cu + and Ag 2+ /Ag + Redox Couples Revisited, J. Phys. Chem. B. 119 (3) (2015) 1152–1163, https://doi.org/10.1021/jp506691h.
[31] M. Fumanal, G. Capano, S. Barthel, B. Smit, I. Tavernelli, Energy-based descriptors for photo-catalytically active metal–organic framework discovery, J. Mater. Chem. A. 8 (8) (2020) 4473–4482, https://doi.org/10.1039/C9TA13506E.
[32] D.I. Kondarides, Photocatalysis, in: Catalysis, Encyclopedia of Life Support Systems (EOLSS), 2005. https://www.eolss.net/sample-chapters/C06/E6-190-16-00.pdf.
[33] M. Fumanal, A. Ortega-Guerrero, K.M. Jablonka, B. Smit, I. Tavernelli, Charge Separation and Charge Carrier Mobility in Photocatalytic Metal-Organic Frameworks, Adv. Funct. Mater. 30 (49) (2020) 2003792, https://doi.org/10.1002/adfm.202003792.
[34] Y. Hinuma, G. Pizzi, Y. Kumagai, F. Oba, I. Tanaka, Band structure diagram paths based on crystallography, Comput. Mater. Sci. 128 (2017) 140–184, https://doi.org/10.1016/j.commatsci.2016.10.015.
[35] W. Yu, D. Xu, T. Peng, Enhanced photocatalytic activity of g-C3N4 for selective CO2 reduction to CH3OH via facile coupling of ZnO: a direct Z-scheme mechanism, J. Mater. Chem. A. 3 (39) (2015) 19936–19947, https://doi.org/10.1039/C5TA05503B.
[36] D. Dubbeldam, S. Calero, D.E. Ellis, R.Q. Snurr, RASPA: Molecular simulation software for adsorption and diffusion in flexible nanoporous materials, Mol. Simul. 42 (2) (2016) 81–101, https://doi.org/10.1080/08927022.2015.1010082.
[37] A.K. Rappe, C.J. Casewit, K.S. Colwell, W.A. Goddard, W.M. Skiff, UFF, a full periodic table force field for molecular mechanics and molecular dynamics simulations, J. Am. Chem. Soc. 114 (25) (1992) 10024–10035, https://doi.org/10.1021/ja00051a040.
[38] J.J. Potoff, J.I. Siepmann, Vapor–liquid equilibria of mixtures containing alkanes, carbon dioxide, and nitrogen, AIChE J. 47 (7) (2001) 1676–1682, https://doi.org/10.1002/aic.690470719.
[39] L. Zhang, J.I. Siepmann, Direct calculation of Henry's law constants from Gibbs ensemble Monte Carlo simulations: nitrogen, oxygen, carbon dioxide and methane in ethanol, Theor. Chem. Acc. 115 (5) (2006) 391–397, https://doi.org/10.1007/s00214-005-0073-1.
[40] L. Zhang, J.I. Siepmann, Development of the trappe force field for ammonia, Collect. Czechoslov. Chem. Commun. 75 (2010) 577–591, https://doi.org/10.1135/cccc2009540.
[41] J.M. Stubbs, Molecular simulations of supercritical fluid systems, J. Supercrit. Fluids. 108 (2016) 104–122, https://doi.org/10.1016/j.supflu.2015.10.027.
[42] E.K. Iskrenova, S.S. Patnaik, Solvent effects in the thermal decomposition reaction of ammonium carbamate: A computational molecular dynamics study of the relative solubilities of CO2 and NH3 in water, ethylene glycol, and their mixtures, Int. J. Heat Mass Transf. 100 (2016) 224–230, https://doi.org/10.1016/j.ijheatmasstransfer.2016.04.050.
[43] M. Wang, T.M. Becker, B.A. Schouten, T.J.H. Vlugt, C.A. Infante Ferreira, Ammonia/ionic liquid based double-effect vapor absorption refrigeration cycles driven by waste heat for cooling in fishing vessels, Energy Convers. Manag. 174 (2018) 824–843, https://doi.org/10.1016/j.enconman.2018.08.060.
[44] P. Ghosh, K.C. Kim, R.Q. Snurr, Modeling Water and Ammonia Adsorption in Hydrophobic Metal-Organic Frameworks: Single Components and Mixtures, J. Phys. Chem. C. 118 (2) (2014) 1102–1110, https://doi.org/10.1021/jp410758t.

[45] L. Huang, T. Bandosz, K.L. Joshi, A.C.T. van Duin, K.E. Gubbins, Reactive adsorption of ammonia and ammonia/water on CuBTC metal-organic framework: A ReaxFF molecular dynamics simulation, J. Chem. Phys. 138 (3) (2013) 034102, https://doi.org/10.1063/1.4774332.
[46] C. Petit, L. Huang, J. Jagiello, J. Kenvin, K.E. Gubbins, T.J. Bandosz, Toward Understanding Reactive Adsorption of Ammonia on Cu-MOF/Graphite Oxide Nanocomposites, Langmuir. 27 (21) (2011) 13043–13051, https://doi.org/10.1021/la202924y.
[47] P.Z. Moghadam, P. Ghosh, R.Q. Snurr, Understanding the Effects of Preadsorbed Perfluoroalkanes on the Adsorption of Water and Ammonia in MOFs, J. Phys. Chem. C. 119 (6) (2015) 3163–3170, https://doi.org/10.1021/jp511835d.
[48] Q.K. Loi, L. Prasetyo, S. Tan, D.D. Do, D. Nicholson, Nonwetting/prewetting/wetting transition of ammonia on graphite, Langmuir. 35 (3) (2019) 641–652, https://doi.org/10.1021/acs.langmuir.8b03634.
[49] P.Z. Moghadam, D. Fairen-Jimenez, R.Q. Snurr, Efficient identification of hydrophobic MOFs: application in the capture of toxic industrial chemicals, J. Mater. Chem. A. 4 (2) (2016) 529–536, https://doi.org/10.1039/C5TA06472D.
[50] M.W. Mahoney, W.L. Jorgensen, A five-site model for liquid water and the reproduction of the density anomaly by rigid, nonpolarizable potential functions, J. Chem. Phys. 112 (20) (2000) 8910–8922, https://doi.org/10.1063/1.481505.
[51] T.F. Willems, C.H. Rycroft, M. Kazi, J.C. Meza, M. Haranczyk, Algorithms and tools for high-throughput geometry-based analysis of crystalline porous materials, Microporous Mesoporous Mater. 149 (1) (2012) 134–141, https://doi.org/10.1016/j.micromeso.2011.08.020.
[52] Accelrys Software Inc., Materials Studio, (2007).
[53] P.G. Boyd, S.M. Moosavi, M. Witman, B. Smit, Force-field prediction of materials properties in metal-organic frameworks, J. Phys. Chem. Lett. 8 (2) (2017) 357–363, https://doi.org/10.1021/acs.jpclett.6b02532.
[54] A.U. Ortiz, A. Boutin, A.H. Fuchs, F.-X. Coudert, Investigating the Pressure-Induced Amorphization of Zeolitic Imidazolate Framework ZIF-8: Mechanical Instability Due to Shear Mode Softening, J. Phys. Chem. Lett. 4 (11) (2013) 1861–1865, https://doi.org/10.1021/jz400880p.
[55] A.A. Emery, J.E. Saal, S. Kirklin, V.I. Hegde, C. Wolverton, High-Throughput Computational Screening of Perovskites for Thermochemical Water Splitting Applications, Chem. Mater. 28 (16) (2016) 5621–5634, https://doi.org/10.1021/acs.chemmater.6b01182.
[56] A.J. Howarth, Y. Liu, P. Li, Z. Li, T.C. Wang, J.T. Hupp, O.K. Farha, Chemical, thermal and mechanical stabilities of metal–organic frameworks, Nat. Rev. Mater. 1 (2016) 15018, https://doi.org/10.1038/natrevmats.2015.18.
[57] G. Mouchaham, S. Wang, C. Serre, The Stability of Metal-Organic Frameworks, in: Met. Fram. Appl. Sep. Catal., 1st ed., Wiley-VCH Verlag GmbH & Co. KGaA, Weinheim, Germany, 2018: pp. 1–28. doi:10.1002/9783527809097.ch1.
[58] P. Nuss, M.J. Eckelman, P.J. Janssen, Life Cycle Assessment of Metals: A Scientific Synthesis, PLoS One. 9 (7) (2014) e101298, https://doi.org/10.1371/journal.pone.0101298.
[59] Thinkstep AG, GaBi 6 software and databases., (2014). http://www.gabi-software.com.
[60] K. Ithisuphalap, H. Zhang, L. Guo, Q. Yang, H. Yang, G. Wu, Photocatalysis and Photoelectrocatalysis Methods of Nitrogen Reduction for Sustainable Ammonia Synthesis, Small Methods. 3 (6) (2019) 1800352, https://doi.org/10.1002/smtd.201800352.
[61] L. Sun, C.H. Hendon, M.A. Minier, A. Walsh, M. Dincă, Million-Fold Electrical Conductivity Enhancement in Fe 2 (DEBDC) versus Mn 2 (DEBDC) (E = S, O), J. Am. Chem. Soc. 137 (19) (2015) 6164–6167, https://doi.org/10.1021/jacs.5b02897.
[62] I.E. Castelli, T. Olsen, S. Datta, D.D. Landis, S. Dahl, K.S. Thygesen, K.W. Jacobsen, Computational screening of perovskite metal oxides for optimal solar light capture, Energy Environ. Sci. 5 (2) (2012) 5814–5819, https://doi.org/10.1039/C1EE02717D.
[63] I.E. Castelli, D.D. Landis, K.S. Thygesen, S. Dahl, I.b. Chorkendorff, T.F. Jaramillo, K.W. Jacobsen, New cubic perovskites for one- and two-photon water splitting using the computational materials repository, Energy Environ. Sci. 5 (10) (2012) 9034, https://doi.org/10.1039/c2ee22341d.
[64] I.E. Castelli, F. Hüser, M. Pandey, H. Li, K.S. Thygesen, B. Seger, A. Jain, K. A. Persson, G. Ceder, K.W. Jacobsen, New Light-Harvesting Materials Using Accurate and Efficient Bandgap Calculations, Adv. Energy Mater. 5 (2) (2015) 1400915, https://doi.org/10.1002/aenm.201400915.
[65] S. Kampouri, F.M. Ebrahim, M. Fumanal, M. Nord, P.A. Schouwink, R. Elzein, R. Addou, G.S. Herman, B. Smit, C.P. Ireland, K.C. Stylianou, Enhanced visible-light-driven hydrogen production through MOF/MOF heterojunctions, ACS Appl. Mater. Interfaces. 13 (12) (2021) 14239–14247, https://doi.org/10.1021/acsami.0c23163.
[66] S. Wang, J.-H. Yun, B. Luo, T. Butburee, P. Peerakiatkhajohn, S. Thaweesak, M. u. Xiao, L. Wang, Recent Progress on Visible Light Responsive Heterojunctions for Photocatalytic Applications, J. Mater. Sci. Technol. 33 (1) (2017) 1–22, https://doi.org/10.1016/j.jmst.2016.11.017.
[67] Q. Xu, L. Zhang, J. Yu, S. Wageh, A.A. Al-Ghamdi, M. Jaroniec, Direct Z-scheme photocatalysts: Principles, synthesis, and applications, Mater. Today. 21 (10) (2018) 1042–1063, https://doi.org/10.1016/j.mattod.2018.04.008.
[68] D. Dokur, S. Keskin, Effects of force field selection on the computational ranking of MOFs for CO_2 separations, Ind. Eng. Chem. Res. 57 (6) (2018) 2298–2309, https://doi.org/10.1021/acs.iecr.7b04792.
[69] J.G. McDaniel, S. Li, E. Tylianakis, R.Q. Snurr, J.R. Schmidt, Evaluation of Force Field Performance for High-Throughput Screening of Gas Uptake in Metal-Organic Frameworks, J. Phys. Chem. C. 119 (6) (2015) 3143–3152, https://doi.org/10.1021/jp511674w.
[70] G.N. Schrauzer, T.D. Guth, Photolysis of Water and Photoreduction of Nitrogen on Titanium Dioxide, J. Am. Chem. Soc. 99 (22) (1977) 7189–7193, https://doi.org/10.1021/ja00464a015.
[71] W. Zhao, J. Zhang, X. Zhu, M. Zhang, J. Tang, M. Tan, Y. Wang, Enhanced nitrogen photofixation on Fe-doped TiO2with highly exposed (101) facets in the presence of ethanol as scavenger, Appl. Catal. B Environ. 144 (2014) 468–477, https://doi.org/10.1016/j.apcatb.2013.07.047.
[72] G.-F. Chen, Y. Yuan, H. Jiang, S.-Y. Ren, L.-X. Ding, L.u. Ma, T. Wu, J. Lu, H. Wang, Electrochemical reduction of nitrate to ammonia via direct eight-electron transfer using a copper–molecular solid catalyst, Nat. Energy. 5 (8) (2020) 605–613, https://doi.org/10.1038/s41560-020-0654-1.
[73] L.R. Redfern, O.K. Farha, Mechanical properties of metal–organic frameworks, Chem. Sci. 10 (46) (2019) 10666–10679, https://doi.org/10.1039/C9SC04249K.
[74] H. Wu, T. Yildirim, W. Zhou, Exceptional Mechanical Stability of Highly Porous Zirconium Metal-Organic Framework UiO-66 and Its Important Implications, J. Phys. Chem. Lett. 4 (6) (2013) 925–930, https://doi.org/10.1021/jz4002345.
[75] K. Banlusan, A. Strachan, First-principles study of elastic mechanical responses to applied deformation of metal-organic frameworks, J. Chem. Phys. 146 (18) (2017) 184705, https://doi.org/10.1063/1.4982356.
[76] V. Colombo, S. Galli, H.J. Choi, G.D. Han, A. Maspero, G. Palmisano, N. Masciocchi, J.R. Long, High thermal and chemical stability in pyrazolate-bridged metal–organic frameworks with exposed metal sites, Chem. Sci. 2 (7) (2011) 1311, https://doi.org/10.1039/c1sc00136a.
[77] A.M. Al-Enizi, J. Ahmed, M. Ubaidullah, S.F. Shaikh, T. Ahamad, M.u. Naushad, G. Zheng, Utilization of waste polyethylene terephthalate bottles to develop metal-organic frameworks for energy applications: A clean and feasible approach, J. Clean. Prod. 248 (2020) 119251, https://doi.org/10.1016/j.jclepro.2019.119251.
[78] W.H. Strehlow, E.L. Cook, Compilation of Energy Band Gaps in Elemental and Binary Compound Semiconductors and Insulators, J. Phys. Chem. Ref. Data. 2 (1) (1973) 163–200, https://doi.org/10.1063/1.3253115.
[79] J. Lee, A. Seko, K. Shitara, K. Nakayama, I. Tanaka, Prediction model of band gap for inorganic compounds by combination of density functional theory calculations and machine learning techniques, Phys. Rev. B. 93 (2016), 115104, https://doi.org/10.1103/PhysRevB.93.115104.